PHYSICAL REVIEW C **90**, 024321 (2014)

Quantum Monte Carlo calculations of electromagnetic transitions in ^{8}Be with meson-exchange currents derived from chiral effective field theory

S. Pastore,[1,*] R. B. Wiringa,[2,†] Steven C. Pieper,[2,‡] and R. Schiavilla[3,4,§]
[1] *Department of Physics and Astronomy, University of South Carolina, Columbia, South Carolina 29208, USA*
[2] *Physics Division, Argonne National Laboratory, Argonne, Illinois 60439, USA*
[3] *Theory Center, Jefferson Laboratory, Newport News, Virginia 23606, USA*
[4] *Department of Physics, Old Dominion University, Norfolk, Virginia 23529, USA*
(Received 9 June 2014; published 25 August 2014)

We report quantum Monte Carlo calculations of electromagnetic transitions in ^{8}Be. The realistic Argonne v_{18} two-nucleon and Illinois-7 three-nucleon potentials are used to generate the ground state and nine excited states, with energies that are in excellent agreement with experiment. A dozen $M1$ and eight $E2$ transition matrix elements between these states are then evaluated. The $E2$ matrix elements are computed only in impulse approximation, with those transitions from broad resonant states requiring special treatment. The $M1$ matrix elements include two-body meson-exchange currents derived from chiral effective field theory, which typically contribute 20%–30% of the total expectation value. Many of the transitions are between isospin-mixed states; the calculations are performed for isospin-pure states and then combined with empirical mixing coefficients to compare to experiment. Alternate mixings are also explored. In general, we find that transitions between states that have the same dominant spatial symmetry are in reasonable agreement with experiments, but transitions between different spatial symmetries are often underpredicted.

DOI: 10.1103/PhysRevC.90.024321 PACS number(s): 21.10.Ky, 02.70.Ss, 23.20.Js, 27.20.+n

I. INTRODUCTION

We recently reported *ab initio* quantum Monte Carlo (QMC) calculations of magnetic moments and electromagnetic (EM) transitions in $A \leqslant 9$ nuclei [1]. In that work, the calculated magnetic moments and $M1$ transitions included corrections arising from EM two-body meson-exchange currents (MECs) derived in two approaches: (i) a standard nuclear physics approximation [2,3] and (ii) the chiral effective theory (χEFT) formulation from Refs. [4–6]. Nuclear wave functions (w.f.'s) were obtained from a Hamiltonian consisting of the nonrelativistic nucleon kinetic energy plus the Argonne v_{18} (AV18) two-nucleon [7] and Illinois-7 (IL7) three-nucleon [8] potentials. The standard nuclear physics approximation MEC were constructed to obey current conservation with this Hamiltonian, while the use of the χEFT MEC constitutes a hybrid calculation. The two methods are in substantial agreement, producing a theoretical microscopic description of nuclear dynamics that successfully reproduces the available experimental data, although the χEFT MEC give somewhat better results. Two-body components in the current operators provide significant corrections to single-nucleon impulse-approximation (IA) calculations. For example, they contribute up to ∼40% of the total predicted value for the ^{9}C magnetic moment [1].

In this work, we implement the framework described above for 20 EM transitions in the ^{8}Be nucleus using only the χEFT MEC. The experimental spectrum and EM transitions we consider are illustrated in Fig. 1. This even-even nucleus exhibits a strong two-α cluster structure in its ground state, characterized by angular momentum, parity, and isospin $(J^{\pi};T) = (0^{+};0)$, and a predominantly [44] Young diagram spatial symmetry. The ground state lies ∼0.1 MeV above the threshold for breakup into two α's, while the $(2^{+};0)$ state at ∼3-MeV excitation and the $(4^{+};0)$ state at ∼11 MeV are [44] rotational states with large (∼1.5- to 3.5-MeV) decay widths. The next six higher states, at 16- to 19-MeV excitation, are three isospin-mixed doublets, with the first pair of $(2^{+};0+1)$ states lying below the threshold for breakup into ^{7}Li + p and having $\alpha+\alpha$ decay widths of ∼100 keV. The isospin mixing is due to the interplay between $T=0$ states and $T=1$ states, which are the isobaric analogs of the lowest three states in ^{8}Li and ^{8}B, all with the same dominant [431] spatial symmetry. There are many additional broad excited states above these isospin-mixed doublets that are not shown before the final state we consider, the $(0^{+};2)$ isobaric analog of the ^{8}He ground state at 27-MeV excitation, with dominant [422] spatial symmetry and a very narrow, 5-keV decay width.

A comprehensive set of QMC calculations of $A=8$ nuclei was carried out in Ref. [9] for a Hamiltonian with AV18 and the older Urbana IX three-nucleon potential [13]. More recently, energies, radii, and quadrupole moments of this nucleus have been recalculated for the [44] symmetry states [10] and for the isospin-mixed states [11], using the newer IL7 potential. The present work complements these studies by calculating many EM transitions between the low-lying states, which are also illustrated in Fig. 1. The $M1$ matrix elements include contributions from two-body χEFT currents, which provide important corrections of the order of 20%–30%. The two-body current corrections to the $E2$ matrix elements are expected to be negligible because they appear at a higher order in the χEFT expansion [6] and are not computed here.

---

[*] pastores@mailbox.sc.edu
[†] wiringa@anl.gov
[‡] spieper@anl.gov
[§] schiavil@jlab.org

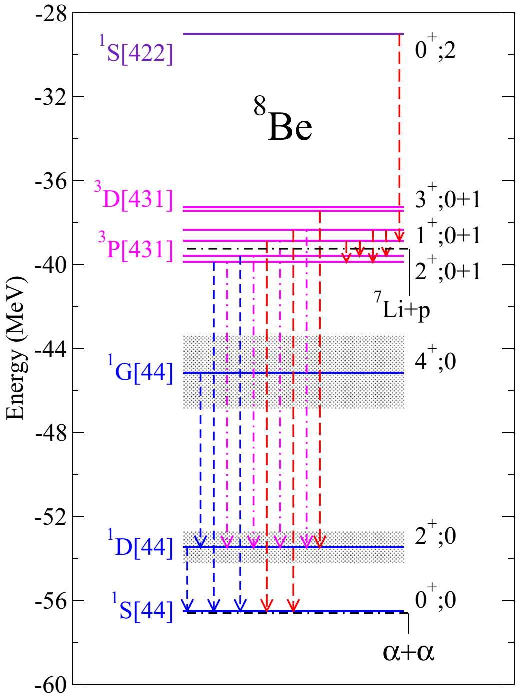

FIG. 1. (Color online) Experimental spectrum of ^{8}Be: horizontal lines denote energy levels, with blue for $T = 0$ states, magenta for mixed $T = 0 + 1$ states, and violet for $T = 2$; black dash-dotted lines indicate thresholds for breakup as indicated and shaded areas denote the large widths of the ^{8}Be rotational states. Vertical lines with arrows indicate the electromagnetic transitions studied: short-dashed (blue) for $E2$, long-dashed (red) for $M1$, and dash-dotted (magenta) for combined $E2$ and $M1$ transitions.

QMC techniques and χEFT EM currents were presented in Ref. [1] and references therein. We refer to that work for more details on the calculational scheme, which is briefly summarized in Sec. II. From there on, we focus on providing and discussing the results. In particular, the calculated ^{8}Be energy spectrum is presented in Sec. III, while results for $E2$ and $M1$ transitions are given in Sec. IV. We discuss the results in Sec. V.

II. QMC METHOD, NUCLEAR HAMILTONIAN, AND χEFT EM CURRENTS

EM transition matrix elements are evaluated between w.f.'s which are solutions of the Schrödinger equation,

$$H\Psi(J^\pi;T,T_z) = E\Psi(J^\pi;T,T_z), \qquad (1)$$

where $\Psi(J^\pi;T,T_z)$ is a nuclear w.f. with specific spin parity J^π, isospin T, and charge state T_z. The nuclear Hamiltonian used in the calculations consists of a kinetic term plus two- and three-body interaction terms, namely, the AV18 [7] and the IL7 [8], respectively:

$$H = \sum_i K_i + \sum_{i<j} v_{ij} + \sum_{i<j<k} V_{ijk}. \qquad (2)$$

Nuclear w.f.'s are constructed in two steps. First, a variational Monte Carlo (VMC) calculation is implemented to construct a trial w.f. $\Psi_V(J^\pi;T,T_z)$ from products of two- and three-body correlation operators acting on an antisymmetric single-particle state of the appropriate quantum numbers. The correlation operators are designed to reflect the influence of the interactions at short distances, while appropriate boundary conditions are imposed at long range [12,13]. The $\Psi_V(J^\pi;T,T_z)$ has embedded variational parameters that are adjusted to minimize the expectation value

$$E_V = \frac{\langle\Psi_V|H|\Psi_V\rangle}{\langle\Psi_V|\Psi_V\rangle} \geqslant E_0, \qquad (3)$$

which is evaluated by Metropolis Monte Carlo integration [14]. Here, E_0 is the exact lowest eigenvalue of H for the specified quantum numbers. A good variational trial function has the form

$$|\Psi_V\rangle = \mathcal{S}\prod_{i<j}^{A}\left[1 + U_{ij} + \sum_{k\neq i,j}^{A} \widetilde{U}_{ijk}^{\rm TNI}\right]|\Psi_J\rangle, \qquad (4)$$

where $\mathcal{S}$ is a symmetrization operator. The Jastrow w.f. Ψ_J is fully antisymmetric and includes all possible spatial symmetry states within the p shell that can contribute to the $(J^\pi;T,T_z)$ quantum numbers of the state of interest, while U_{ij} and $\widetilde{U}_{ijk}^{\rm TNI}$ are the noncommuting two- and three-body correlation operators.

The second step improves on Ψ_V by eliminating excited-state contamination. This is accomplished by the Green's function Monte Carlo (GFMC) algorithm [15], which propagates the Schrödinger equation in imaginary time (τ). The propagated w.f., $\Psi(\tau) = e^{-(H-E_0)\tau}\Psi_V$, for large values of τ converges to the exact w.f. with eigenvalue E_0. In practice, a simplified version H' of the Hamiltonian H is used in the operator, which includes the isoscalar part of the kinetic energy, a charge-independent eight-operator projection of AV18 called AV8$'$, a strength-adjusted version of the three-nucleon potential IL7$'$ (adjusted so that $\langle H'\rangle \sim \langle H\rangle$), and an isoscalar Coulomb term that integrates to the total charge of the given nucleus [16]. The difference between H and H' is calculated using perturbation theory. More details can be found in Refs. [9] and [13].

Matrix elements of the operators of interest are evaluated in terms of a "mixed" expectation value between Ψ_V and $\Psi(\tau)$:

$$\langle O(\tau)\rangle_M = \frac{\langle\Psi(\tau)|O|\Psi_V\rangle}{\langle\Psi(\tau)|\Psi_V\rangle}, \qquad (5)$$

where the operator O acts on the trial function Ψ_V. The desired expectation values, of course, have $\Psi(\tau)$ on both sides; by writing $\Psi(\tau) = \Psi_V + \delta\Psi(\tau)$ and neglecting terms of order $[\delta\Psi(\tau)]^2$, we obtain the approximate expression

$$\begin{aligned}\langle O(\tau)\rangle &= \frac{\langle\Psi(\tau)|O|\Psi(\tau)\rangle}{\langle\Psi(\tau)|\Psi(\tau)\rangle} \\ &\approx \langle O(\tau)\rangle_M + [\langle O(\tau)\rangle_M - \langle O\rangle_V],\end{aligned} \qquad (6)$$

where $\langle O\rangle_{\rm V}$ is the variational expectation value.

For off-diagonal matrix elements relevant to this work the generalized mixed estimate is given by the expression

$$\frac{\langle\Psi^f(\tau)|O|\Psi^i(\tau)\rangle}{\sqrt{\langle\Psi^f(\tau)|\Psi^f(\tau)\rangle}\sqrt{\langle\Psi^i(\tau)|\Psi^i(\tau)\rangle}} \approx \langle O(\tau)\rangle_{M_i}+\langle O(\tau)\rangle_{M_f}-\langle O\rangle_V, \tag{7}$$

where

$$\langle O(\tau)\rangle_{M_f} = \frac{\langle\Psi^f(\tau)|O\big|\Psi^i_V\big\rangle}{\langle\Psi^f(\tau)\big|\Psi^f_V\big\rangle}\sqrt{\frac{\big\langle\Psi^f_V|\Psi^f_V\big\rangle}{\big\langle\Psi^i_V|\Psi^i_V\big\rangle}} \tag{8}$$

and $\langle O(\tau)\rangle_{M_i}$ is defined similarly. For more details see Eqs. (19)–(24) and the accompanying discussions in Ref. [17]. Sources of systematic error in the GFMC evaluation of operator expectation values (other than H') include the use of mixed estimates and the constrained path algorithm for controlling the Fermion sign problem in the propagation of $\Psi(\tau)$. These are discussed in Ref. [9]; the convergence of the current calculations is addressed at the beginning of Sec. III.

Nuclear EM currents are expressed as an expansion in many-body operators. The current we use contains up to two-body effects and is written as

$$\mathbf{j}(\mathbf{q}) = \sum_i \mathbf{j}_i(\mathbf{q}) + \sum_{i<j}\mathbf{j}_{ij}(\mathbf{q}), \tag{9}$$

where $\mathbf{q}$ is the momentum associated with the external EM field. In what follows, we use the notation

$$\begin{aligned}\mathbf{k}_i &= \mathbf{p}_i' - \mathbf{p}_i, \quad \mathbf{K}_i = (\mathbf{p}_i' + \mathbf{p}_i)/2,\\ \mathbf{k} &= (\mathbf{k}_1 - \mathbf{k}_2)/2, \quad \mathbf{K} = \mathbf{K}_1 + \mathbf{K}_2,\end{aligned} \tag{10}$$

where $\mathbf{p}_i$ ($\mathbf{p}_i'$) is the initial (final) momentum of nucleon i, and $\mathbf{q} = \mathbf{k}_1 + \mathbf{k}_2$ by momentum conservation.

There are two one-body operators resulting from retaining the first two terms in the $(\mathbf{p}_i/m_N)^2$ expansion of the covariant single-nucleon EM current. Of course, the leading-order (LO) term in this expansion corresponds to the nonrelativistic IA operator consisting of the convection and spin-magnetization single-nucleon currents,

$$\mathbf{j}_i^{\rm IA} = \frac{e}{2m_N}[2e_{N,i}\mathbf{K}_i + i\mu_{N,i}\boldsymbol{\sigma}_i\times\mathbf{q}], \tag{11}$$

for nucleon i, and where

$$\begin{aligned}e_{N,i} &= (1+\tau_{iz})/2\,, \quad \kappa_{N,i} = (\kappa_S + \kappa_V\tau_{iz})/2\,,\\ \mu_{N,i} &= e_{N,i} + \kappa_{N,i}.\end{aligned} \tag{12}$$

Here $\kappa_S = -0.12$ and $\kappa_V = 3.706$ are the isoscalar (IS) and isovector (IV) combinations of the anomalous magnetic moments of the proton and neutron, and e is the electric charge.

Two-body EM currents are constructed from a χEFT which retains both pions and nucleons as explicit degrees of freedom. The resulting operators are expressed as an expansion in nucleon and pion momenta, generically designated Q. The LO contribution in Eq. (11) is of order $e\,Q^{-2}$ and contributions up to next-to-next-to-leading order (N3LO) or $e\,Q^1$ are retained in the expansion. These contributions were first calculated by Park *et al.* in Ref. [18] using covariant perturbation theory. More recently, Kölling and collaborators [19], as well as some of the present authors [4–6,20], derived them using two different implementations of time-ordered perturbation theory. In this work, we use the operators developed in Refs. [4–6] and [20], where details on the derivation and a complete listing of the formal expressions may be found.

The two-body χEFT EM currents consist of long- and intermediate-range components described in terms of one-pion exchange (OPE) and two-pion exchange (TPE) contributions, respectively, as well as contact currents encoding short-range dynamics. In particular, OPE seagull and pion-in-flight currents appear at next-to-leading order (NLO) ($e\,Q^{-1}$) in the Q expansion, while TPE currents occur at N3LO. The LO and next-to-next-to-leading order (N2LO) ($e\,Q^0$) contributions are given by the single-nucleon operators described above, i.e., the IA operator and its relativistic correction, respectively.

At N3LO, the current operators involve a number of unknown low-energy constants (LECs) which are fixed to experimental data. The LECs multiplying four-nucleon contact operators are of two kinds, namely, minimal and nonminimal. The former also enter the χEFT nucleon-nucleon potential at order Q^2 and are therefore fixed by reproducing the np and pp elastic scattering data, along with the deuteron binding energy. For these, we take the values resulting from the fitting procedure implemented in Refs. [21] and [22]. Nonminimal LECs (there are two of them, one multiplying an isoscalar operator and the other an isovector operator) need to be fixed to EM observables.

At N3LO, there is also an additional current of one-pion range which involves three LECs. One of these multiplies an isoscalar structure, while the remaining two multiply isovector structures. As first observed in Ref. [18], the isovector component of this current has the same operator structure as that associated with a Δ-resonance transition current involving an OPE. In this type of two-body contribution, the external photon couples with a nucleon to excite a Δ-resonance state. The latter decays, emitting a pion which is then reabsorbed by a second nucleon. Given this theoretical insight, one can impose the condition that the two isovector LECs are in fact given by the couplings of the Δ-resonance current. This mechanism is referred to as Δ-resonance saturation and has been utilized in various studies of EM observables of light nuclei (see, for example, [1,6], and [23–26]). Once the Δ-saturation mechanism is invoked to fix two of the unknown LECs, the remaining three LECs are fit to the deuteron and the trinucleon magnetic moments.

The values of the LECs are not unique, in that they depend on the particular momentum cutoff used to regularize the configuration-space singularities of the EM operators. In momentum space, these operators have a power-law behavior for large momenta, k, which is regularized by a momentum cutoff of the form $C(k) = \exp(-k^4/\Lambda^4)$. For a list of the numerical values of the LECs for $\Lambda = 600$ MeV, which is the cutoff utilized in these calculations, we refer to Ref. [1].

The N2LO relativistic correction to the one-body IA operator involves two derivatives acting on the nucleon field. In the GFMC calculation we do not explicitly evaluate this p_i^2 term but, instead, approximate it with its average value, that is, $p_i^2 \sim \langle p_i^2\rangle$, as determined from the expectation value of the kinetic energy operator in ^{8}Be, from which we obtain

$\langle p_i^2 \rangle = 1.375$ fm^{-2}. This term is a small fraction of the total MEC (see, e.g., Table IV below) so the approximation has little practical effect.

To be consistent with the nomenclature utilized in Ref. [1], we denote by MEC components in the EM currents beyond the IA one-body operator at LO. However, we stress that the N2LO contribution is a one-body operator, which does not involve meson-exchange mechanisms.

III. ^{8}BE ENERGY SPECTRUM

The experimental [27] and calculated GFMC energies for the ^{8}Be spectrum are listed in Table I, along with the GFMC point proton radii. The calculations were done by propagating up to some $\tau_{\max}$, with an evaluation of observables after every 40 propagation steps, i.e., at intervals of $\tau = 0.02$ MeV^{-1}, and averaging in the interval $\tau = [(0.1\ \text{MeV}^{-1})\text{–}\tau_{\max}]$; $\tau_{\max}$ is typically 0.3 to 0.4 MeV^{-1}.

The calculation of the spectrum is rather involved [9], with two main challenges to face. The first originates from the resonant nature of the first two excited states [shaded (gray) states in Fig. 1], and the ensuing difficulty of extracting a stable resonance energy from the calculated energies, which are evolving to the energy of two separated α's. This issue was addressed in Ref. [9] and more recently, however succinctly, in Ref. [10]. The last reference reported an updated measurement of the $E2$ transition between the first two excited states of ^{8}Be measured via the $\alpha + \alpha$ radiative capture with an uncertainty of ~10% (as opposed to the estimated ~30% error of previous measurements [28]). To accompany the experimental result, a GFMC calculation was performed for the $E2$ transition matrix element between the two rotational states and between the $(2^+;0)$ state and the ground state. We reprise this calculation in more detail below.

The second nontrivial issue is encountered when dealing with the spectrum of the isospin-mixed states at 16–19 MeV (magenta states in Fig. 1). These excited states have been extensively discussed in Ref. [11]. We compute unmixed $T = 0$ or $T = 1$ states, but experimental values are, of course, for the mixed states. The isospin-mixing coefficients can be extracted from experimental decay widths [29]. For the 2^+ multiplet this is unambiguous, but for the 1^+ and 3^+ multiplets theoretical decay widths based on shell-model calculations have been used. This is discussed further below. In Table I we use the mixing parameters to unfold the "empirical" pure-isospin energies for comparison with our calculations, while in subsequent tables we fold the computed EM matrix elements to generate mixed matrix elements to compare to the data.

We studied the convergence of the GFMC calculations with respect to variations in the number of unconstrained steps ($n_u = 20$ and 50) followed after the path constraint is relaxed, and found that energies, magnetic moments, and rms radii converge at $n_u = 20$, which is used for the final results reported here. Most of the calculations we present are obtained by averaging two calculations, each using 50 000 walkers. For the physically narrow, nonresonant states, the energy expectation value is seen to stabilize at $\tau \sim 0.1$ MeV^{-1}.

For the physically wide, resonant states, the binding energy, magnitude of the quadrupole moment, and point proton radius all increase monotonically as τ increases. We interpret this as an indication that the system is dissolving into two separated α's. In Fig. 2, we show the GFMC propagation points for the energy expectation values of the first three states of ^{8}Be. In particular, the ground-state energy is obtained with $n_u = 20$ and 20 000 walkers, while the resonant state energies are obtained using $n_u = 20$ and averaging two calculations with 50 000 walkers each. From the figure, we see that the ground-state initial VMC energy expectation value at $\tau = 0$ quickly drops and reaches stability around $\tau = 0.1$ MeV^{-1} (this point is indicated in the figure by an open star). The energies of the two resonant states, instead, keep falling with time: the $(2^+;0)$ state decreases 0.25 MeV over the interval $\tau = [0.1, 0.3]$ MeV^{-1}, while the $(4^+;0)$ state falls by 1 MeV. With this declining energy there is a corresponding increase in

TABLE I. GFMC ground-state energy and excitations (in MeV) for the AV18 + IL7 Hamiltonian compared to experiment [27] for the ^{8}Be spectrum. Empirical energies are obtained by unfolding the isospin-mixed experimental energies using inferred mixing coefficients (see text for explanation). Also listed are the GFMC point proton (=neutron) radii (in fm). Theoretical or experimental errors $\geqslant$1 in the last digit are given in parentheses.

$J^\pi;T$	GFMC	Empirical	Experimental	r_p
0^+	–56.3(1)		–56.50	2.40
2^+	+3.2(2)		+3.03(1)	2.45(1)
4^+	+11.2(3)		+11.35(15)	2.48(2)
$2_2^+;0$	+16.8(2)	+16.746(3)	+16.626(3)	2.28
$2^+;1$	+16.8(2)	+16.802(3)	+16.922(3)	2.33
$1^+;1$	+17.5(2)	+17.66(1)	+17.640(1)	2.39
$1^+;0$	+18.0(2)	+18.13(1)	+18.150(4)	2.36
$3^+;1$	+19.4(2)	+19.10(3)	+19.07(3)	2.31
$3^+;0$	+19.9(2)	+19.21(2)	+19.235(10)	2.35
$0^+;2$	+27.7(2)		+27.494(2)	2.58

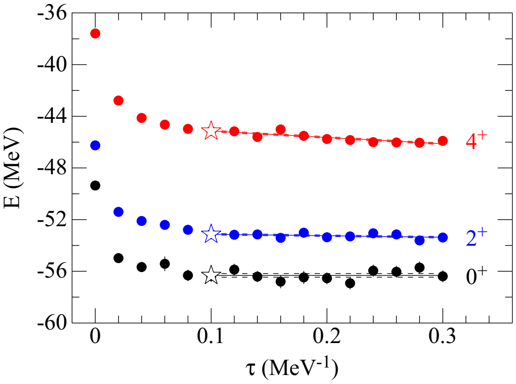

FIG. 2. (Color online) GFMC propagation in imaginary time τ of the energy expectation values of the first three states in the ^{8}Be spectrum. Lower black circles represent GFMC propagation points for the ground state; middle (blue) circles, the $(2^+;0)$ rotational state at ~3-MeV excitation; and upper (red) circles, the $(4^+;0)$ state at ~11-MeV excitation. Solid lines represent a linear fit to the GFMC points in the indicated time interval and dashed lines show a one-standard-deviation Monte Carlo statistical error for the fit.

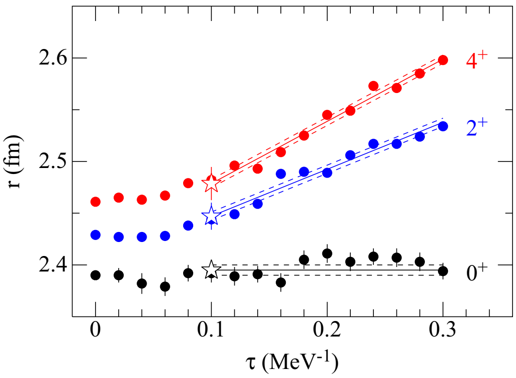

FIG. 3. (Color online) GFMC propagation in imaginary time τ of the point proton radius expectation values of the first three states in the ^{8}Be spectrum; notation is the same as for Fig. 2.

the point proton radius expectation values, as shown in Fig. 3 and in the magnitude of the (negative) electric quadrupole moment.

Quantities associated with the resonant states have been calculated assuming that, also for these states, $\tau \sim 0.1\ \text{MeV}^{-1}$ is the point at which spurious contamination in the nuclear w.f.'s has been eliminated by the GFMC propagation. Thus, we make a linear fit to the GFMC values in the interval $\tau = [0.1,0.3]\ \text{MeV}^{-1}$ and extrapolate to $\tau = 0.1\ \text{MeV}^{-1}$ for the reported values. The choice of $\tau = 0.1\ \text{MeV}^{-1}$ is somewhat arbitrary. To account for this uncertainty we increase the GFMC statistical error by a systematic error that is obtained by studying the sensitivity of the results with respect to fitting procedures implemented in two different intervals, namely, $\tau = [0.08,0.3]\ \text{MeV}^{-1}$ and $\tau = [0.12,0.3]\ \text{MeV}^{-1}$, while keeping the same extrapolating point. The total error is represented in the figures by dashed lines.

For the six states at 16- to 19-MeV excitation, the GFMC calculations are done for pure isospin states of either $T = 0$ or $T = 1$. The w.f.'s of the isospin-mixed states are written as

$$\begin{aligned}\Psi_J^a &= \alpha_J \Psi_{J,T=0} + \beta_J \Psi_{J,T=1},\\ \Psi_J^b &= \beta_J \Psi_{J,T=0} - \alpha_J \Psi_{J,T=1},\end{aligned} \tag{13}$$

where the mixing angles satisfy $\alpha_J^2 + \beta_J^2 = 1$. As one can see from Fig. 1 and Table I, experimentally there are two $J^\pi = 2^+$ isospin-mixed states, at 16.626- and 16.922-MeV excitation energies; two $J^\pi = 1^+$ states, at 17.64 and 18.15 MeV; and two $J^\pi = 3^+$ states, at 19.07 and 19.235 MeV. The mixing angles are inferred from the experimental values of the decay widths. We follow the analysis carried out by Barker in Ref. [29] and update the experimental widths with more recent values to obtain the following mixing coefficients [11]:

$$\begin{aligned}\alpha_2 &= 0.7705(15), \quad \beta_2 = 0.6375(19),\\ \alpha_1 &= 0.21(3), \quad \beta_1 = 0.98(1),\\ \alpha_3 &= 0.41(10), \quad \beta_3 = 0.91(5).\end{aligned} \tag{14}$$

Mixing coefficients for the 2^+ states are well known because for these states there is only one decay channel energetically open, that is, the 2α emission channel, for which the experimental widths are known with ~0.5% accuracy. For the other isospin-mixed states, multiple decay channels are available, which makes the extraction of the mixing coefficients less direct. In addition, theoretical values of $M1$ matrix elements must be used; the values above were obtained using the traditional shell model without two-body current contributions to the matrix elements [11,29]. Revised mixing parameters for the 1^+ pair, computed using the $M1$ matrix elements developed here, are discussed in Sec. V.

The eigenenergies of the isospin-mixed states listed in Table I are given by

$$E_{a,b} = \frac{H_{00} + H_{11}}{2} \pm \sqrt{\left(\frac{H_{00} - H_{11}}{2}\right)^2 + (H_{01})^2}, \tag{15}$$

where H_{00} is the diagonal energy expectation in the pure $T = 0$ state, H_{11} is the expectation value in the $T = 1$ state, and H_{01} is the off-diagonal isospin-mixing matrix element that connects $T = 0$ and $T = 1$. The inferred H_{00} and H_{11} are the empirical values listed in Table I.

Finally, the narrow $(0^+;2)$ state at 27-MeV excitation, which has a dominant [422] spatial symmetry, is a straightforward GFMC calculation. There could, in principle, be isospin mixing with the third $(0_3^+;0)$ state in the p-shell construction of ^{8}Be, which also has [422] symmetry, via the EM and charge-dependent parts of the AV18. No such state has been identified experimentally. The first VMC calculation places this state 0.7(1) MeV higher in excitation, with a 125-keV isospin-mixing matrix element, which predicts $\alpha_0 = 0.19(4)$ and $\beta_0 = 0.98(1)$. This small amount of mixing may still have a moderate effect on the width of the physical state, as discussed below.

The overall agreement between experiment and the calculated GFMC spectrum for AV18 + IL7 listed in Table I is excellent. Only the 3^+ isospin-mixed doublet is a little too high in excitation and a little too spread out compared to the measured values.

IV. ELECTROMAGNETIC TRANSITIONS IN ^{8}BE

We present our results in terms of reduced matrix elements (using Edmonds' convention) of the $E2$ and $M1$ operators, the associated $B(E2)$ and $B(M1)$, and the resulting widths. For a transition of multipolarity λ (X designates E or M),

$$B(X\lambda) = \langle \Psi_{J_f} || X\lambda || \Psi_{J_i} \rangle^2 / (2J_i + 1) \tag{16}$$

is in units of $e^\lambda\ \text{fm}^{2\lambda}$ for electric transitions and $(\mu_N)^{2\lambda}$ for magnetic transitions. The widths are given by

$$\Gamma_{X\lambda} = \frac{8\pi(\lambda+1)}{\lambda[(2\lambda+1)!!]^2} \alpha \hbar c \left(\frac{\Delta E}{\hbar c}\right)^{2\lambda+1} B(X\lambda), \tag{17}$$

where ΔE is the difference in MeV between the experimental initial- and final-state energies, E_i and E_f; α is the fine-structure constant; and $\hbar c$ is in units of MeV fm.

The calculations of EM matrix elements have been described in detail in Refs. [2] and [17]. Our present results for $E2$ transitions in ^{8}Be are listed in Table II, where the initial and final $(J^\pi;T)$ states and the dominant associated spatial symmetries are shown in the first column and the reduced matrix elements between states of pure isospin are given in the second column. The experimental energies for the physical

TABLE II. Calculated reduced $E2$ matrix elements and corresponding decay widths compared to experiment [10,27]. From left to right, the columns show (1) the initial and final $(J^\pi;T)$ states and the dominant associated spatial symmetries, (2) the GFMC matrix elements between states of pure isospin, (3) the experimental energies, and (4) the isospin-mixed theoretical and (5) experimental widths. For the width values we use the notation $[-x] = 10^{-x}$.

$(J_i^\pi;T_i) \to (J_f^\pi;T_f)$,	$E2$		Γ_{E2} (eV)	
$[\text{s.s.}]_i \to [\text{s.s.}]_f$	(e fm^2)	E_i (MeV) $\to$ E_f (MeV)	IA	Expt.
$(2^+;0) \to (0^+;0)$	10.0(2)	3.03 → 0.	4.12(16)[-3]	–
$(4^+;0) \to (2^+;0)$	15.6(4)	11.35 → 3.03	0.87(5)	0.67(7)
[44] → [44]				
$(2_2^+;0) \to (0^+;0)$	0.55(11)	16.626 → 0.	1.6(1.0)[–2]	7.0(2.5)[–2]
$(2^+;1) \to (0^+;0)$	–0.23(2)	16.922 → 0.	6.2(2.0)[–2]	8.4(1.4)[–2]
[431] → [44]				
$(2_2^+;0) \to (2^+;0)$	0.26(7)	16.626 → 3.03	3.6(2.2)[–3]	–
$(2^+;1) \to (2^+;0)$	0.03(2)	16.922 → 3.03	1.7(1.4)[–3]	–
[431] → [44]				
$(1^+;1) \to (2^+;0)$	1.93(6)	17.64 → 3.03	0.63(5)	0.12(5)
$(1^+;0) \to (2^+;0)$	–0.03(5)	18.15 → 3.03	4.0(1.1)[–2]	–
[431] → [44]				

states are given in the third column, and the corresponding theoretical and experimental widths are listed in the fourth and fifth columns. We use the IA operator

$$E2 = e\sum_k \frac{1}{2}\left[r_k^2 Y_2(\hat{r}_k)\right](1+\tau_{kz}) \tag{18}$$

without any MEC corrections.

In previous calculations [1,17,30] of nuclei in the $A = 6$–10 range, we have found that $E2$ matrix elements of narrow states are generally quite stable under GFMC propagation and seldom vary much from the initial VMC estimate. However, matrix elements from wide states, e.g., for the ^{6}Li $(2^+;0) \to (0^+;0)$ decay, show a significant evolution as a function of τ. This is also true for the first two transitions in ^{8}Be from the broad rotational 2^+ and 4^+ states. The matrix element grows monotonically as the GFMC solution evolves in τ toward a separated $\alpha+\alpha$ configuration, as illustrated in Fig. 4. This growth is slow for the lower $(2^+;0) \to (0^+;0)$ transition but much more pronounced for the upper $(4^+;0) \to (2^+;0)$ transition. Consequently, we make an extrapolation back to $\tau = 0.1 \pm 0.02$ MeV^{-1} to obtain our best estimate for the matrix element, just as we did for the energy and point proton radius discussed above in conjunction with Figs. 2 and 3. Our error estimate combines both the Monte Carlo statistical error and the uncertainty in the extrapolation point. The numerical results for these two matrix elements and corresponding decay widths Γ_{E2} are reported at the top of Table II. The transitions, which are between states of the same dominant [44] spatial symmetry, are very large and consistent with a rotor picture for ^{8}Be.

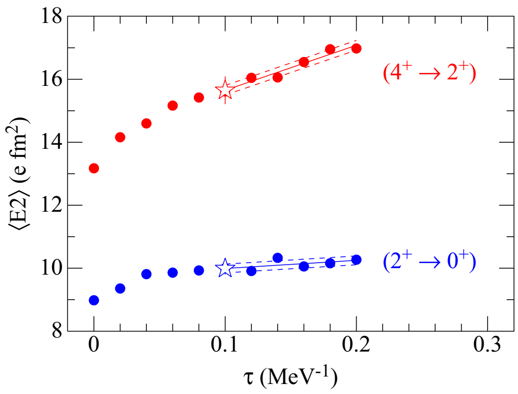

FIG. 4. (Color online) GFMC propagation in imaginary time τ of the reduced $E2$ matrix elements among the first three states in the ^{8}Be spectrum; upper (red) circles represent the $(4^+;0) \to (2^+;0)$ transition; lower (blue) circles, the $(2^+;0) \to (0^+;0)$ transition; and open stars, the extrapolated values.

We have also calculated an additional six $E2$ transitions from the isospin-mixed 2^+ and 1^+ doublets with dominant [431] spatial symmetry to the $T = 0$ ground state or first 2^+ state. We denote the isospin-pure matrix elements $E2_{T_fT_i} = \langle\Psi_{J_f,T_f}||E2||\Psi_{J_i,T_i}\rangle$ and then use the definitions given in Eq. (13) to combine them via

$$\begin{aligned}\left\langle\Psi_{J_f,0}\middle|\middle|E2\middle|\middle|\Psi^a_{J_i}\right\rangle &= \alpha_{J_i}E2_{00} + \beta_{J_i}E2_{01},\\ \left\langle\Psi_{J_f,0}\middle|\middle|E2\middle|\middle|\Psi^b_{J_i}\right\rangle &= \beta_{J_i}E2_{00} - \alpha_{J_i}E2_{01}\end{aligned} \tag{19}$$

to evaluate the widths of the physical transitions for comparison to experiment. Because the $E2$ operator largely preserves spatial symmetry, these transitions are much weaker than the ones within the α-α rotational band. This makes accurate calculations of these transitions significantly more difficult.

As an example, we can compare the two $E2$ transitions from the first and second 2^+ states to the 0^+ ground state. As discussed in Refs. [31] and [32], the 0^+ state has five contributing LS-coupled symmetry components, $^1S[44]$, $^3P[431]$, $^5D[422]$, $^1S[422]$, and $^3P[4211]$, with the first component having an amplitude in the present VMC starting w.f. of 0.996. The 2^+ states are linear combinations of eight components: $^1D[44]$, $^3P[431]$, $^3D[431]$, $^3F[431]$, $^5S[422]$, $^5D[422]$, $^1D[422]$, and $^3P[4211]$. The first 2^+ state also has an amplitude of 0.996 from the $^1D[44]$ component, while the second 2^+ state is dominated by the $^3P[431]$ component with an amplitude of 0.902. Consequently, 99% of the large $E2$ transition from the first excited state to the ground state is due to the matrix element between the $^1D[44]$ and the $^1S[44]$ components. However, for the much smaller $E2$ transition from the second 2^+ state, this pair of components contributes 1.65 times the final result, canceled by the matrix element between the two $^3P[431]$ components, which gives -1.44 times the final result. The remaining 38 smaller terms, among which there is much additional cancellation, give 80% of the total.

Changes in these small components, which may have little effect on the energy of a given state and hence are not highly constrained by the GFMC propagation, can have a significant effect on the $E2$ matrix element. These small components may also be rather sensitive to the three-body potential in the Hamiltonian, as noted in an earlier study of $E2$ transitions in $A = 10$ nuclei [30]. This is also true for many of the $M1$ transitions discussed below, when the initial and final states have different dominant spatial symmetries.

An additional complication arises for transitions from the second 2^+ state because the GFMC propagation is not guaranteed to preserve the orthogonality of the w.f. relative to the first 2^+ state. In practice, GFMC propagation starting from orthogonal VMC w.f.'s preserves the orthogonality to a high degree [31]; in this case the amplitude $\langle \Psi^{2_2^+}(\tau) | \Psi_V^{2+} \rangle$ increases from 0.0010(7) for $\tau = 0$ to 0.040(6) averaged over $0.1 \leqslant \tau \leqslant 0.3$. This small admixture leaves the energy and point proton radius of the second 2^+ state as stable functions of τ, as expected for a narrow state. However, for the $E2$ matrix element from the 2_2^+ state to states of dominant [44] symmetry, there are the large cancellations discussed above and a small admixture of the the 2^+ state with its large $E2$ matrix element to states of dominant [44] symmetry can substantially affect the overlap. For this reason we have applied a correction by orthogonalizing the $\Psi^{2_2^+}(\tau)$ to Ψ_V^{2+},

$$\Psi^{2_2^{+\prime}}(\tau) = \Psi^{2_2^+}(\tau) - \left\langle \Psi^{2_2^+}(\tau) \middle| \Psi_V^{2+} \right\rangle \Psi^{2^+}(\tau) . \tag{20}$$

This reduces the mixed estimates $\langle \Psi^{2_2^+}(\tau) | E2 | \Psi_V^{2+} \rangle$ by 50% and $\langle \Psi^{2_2^+}(\tau) | E2 | \Psi_V^{0+} \rangle$ by 20%. This correction is also made for corresponding $M1$ transitions discussed below but is relatively much less important.

For the $M1$ transitions the IA matrix element is evaluated using the $M1$ operator induced by the one-body current given in Eq. (11), namely,

$$\boldsymbol{\mu}^{\rm IA} = \sum_{i=1}^{A} (e_{N,i}\, \mathbf{L}_i + \mu_{N,i}\, \boldsymbol{\sigma}_i), \tag{21}$$

while the one-body current at N2LO generates the additional M1 operator terms [4]

$$\boldsymbol{\mu}^{\rm N2LO} = -\frac{e}{8\, m_N^3} \sum_{i=1}^{A} \big[\{ p_i^2 , e_{N,i}\, \mathbf{L}_i + \mu_{N,i}\, \boldsymbol{\sigma}_i \} + e_{N,i}\, \mathbf{p}_i \times (\boldsymbol{\sigma}_i \times \mathbf{p}_i) \big], \tag{22}$$

where $\mathbf{p}_i = -i \nabla_i$ and $\mathbf{L}_i$ are the linear momentum and angular momentum operators of particle i, and $\{\ldots , \ldots\}$ denotes the anticommutator.

The matrix element associated with the contribution of two-body currents is

$$\left\langle J_f^\pi , M_f \middle| \mu_z^{\rm MEC} \middle| J_i^\pi , M_i \right\rangle = -i \lim_{q \to 0} \frac{2\, m_N}{q} \left\langle J_f^\pi , M_f \middle| j_y^{\rm MEC}(q\, \hat{\mathbf{x}}) \middle| J_i^\pi , M_i \right\rangle, \tag{23}$$

where the spin-quantization axis and momentum transfer $\mathbf{q}$ are, respectively, along the $\hat{\mathbf{z}}$ and $\hat{\mathbf{x}}$ axes, and $M_f = M_i$. The various contributions are evaluated for two small values of $q < 0.02$ fm^{-1} and then extrapolated linearly to the limit $q = 0$. The error due to extrapolation is much smaller than the statistical error in the Monte Carlo sampling.

In Table III, we report the results for the $M1$ transition matrix elements as well as the decay widths Γ_{M1} between the low-lying excited states. The first column specifies the initial and final states of pure isospin. The second column, labeled "IA," shows the IA results obtained with the transition operator of Eq. (21), while the third column, labeled "Total" lists results obtained with the complete EM current operator, Eqs. (21)–(23). The percentage of the total matrix element given by the MEC contributions is shown in the fourth column. The fifth column reports the energies of the physical states, while the last three columns compare the corresponding widths with the experimental data from Ref. [27].

As observed in Ref. [1], IA matrix elements are found to have larger statistical fluctuations than MEC matrix elements. We separately compute IA and MEC matrix elements and then sum the resulting values to obtain the total numbers.

It is worthwhile noting that M1 transitions involving the resonant states do not monotonically change as τ increases, a behavior unlike the quadrupole moments, point proton radii, and energies of these states. This stability is understood by observing that the (2^+;0) and (4^+;0) rotational states in ^{8}Be are $\sim$99% pure $^1D_2[44]$ and $^1G_4[44]$ states, so they are quantized with $L = 2$ and $L = 4$, respectively. The orbital contribution to the magnetic moment is just $L/2\ \mu_N$ because only protons contribute; i.e., it is equal to 1.00 μ_N in the (2^+;0) state and 2.00 μ_N in the (4^+;0) state. Because it is quantized, the magnetic moment should not vary as the nucleus starts to break up in the GFMC propagation, unlike the point proton radius, where r grows as τ increases. Due to this stability, we can safely propagate $M1$ matrix elements involving resonant states to larger values of τ and average the GFMC result in larger τ intervals.

As for the $E2$ transitions above, the $M1$ matrix elements are evaluated between states with a well-defined isospin, $T = 0$ or 1. We denote these matrix elements $M1_{T_f T_i} = \langle \Psi_{J_f,T_f} || \mu || \Psi_{J_i,T_i} \rangle$, with T_f and T_i equal to 0 or 1. For transitions involving isospin mixing in the initial or final state, we use expressions similar to Eq. (19) to generate the physical transition rates. For transitions in which both the initial and the final states are isospin mixed, using the definitions given in Eq. (13), we obtain the following expressions for the

TABLE III. Calculated reduced $M1$ matrix elements and corresponding decay widths compared to experiment [27]. From left to right, the columns show (1) the initial and final $(J^\pi;T)$ states and the dominant associated spatial symmetries, (2) the GFMC matrix elements between states of pure isospin in IA and (3) in total after adding MEC, (4) the percentage z of the total given by the MEC, (5) the experimental energies, (6) the isospin-mixed theoretical decay widths in IA and (7) in total, and (8) the experimental values. In the width values we use the notation $[-x] = 10^{-x}$. Results followed by a superscript asterisk or dagger are extra VMC calculations discussed in the text.

$(J_i;T_i) \to (J_f;T_f)$,	$M1$ (μ_N)				Γ_{M1} (eV)		
$[\text{s.s.}]_i \to [\text{s.s.}]_f$	IA	Total	z	E_i (MeV) $\to$ E_f (MeV)	IA	Total	Expt.
$(2_2^+;0) \to (2^+;0)$	0.014(6)	0.013(6)		$16.626 \to 3.03$	0.23(3)	0.51(6)	
$(2^+;1) \to (2^+;0)$	0.297(12)	0.447(18)	33%	$16.922 \to 3.03$	0.30(4)	0.70(7)	
$[431] \to [44]$				$16.626 + 16.922 \to 3.03$	0.53(5)	1.21(9)	2.80(18)
$(1^+;1) \to (0^+;0)$	0.551(7)	0.767(9)	28%	$17.64 \to 0.00$	6.2(2)	12.0(3)	15.0(1.8)
$(1^+;1) \to (2^+;0)$	0.398(6)	0.567(11)	30%	$17.64 \to 3.03$	1.9(1)	3.8(2)	6.7(1.3)
$(1^+;0) \to (0^+;0)$	0.012(1)	0.014(1)		$18.15 \to 0.00$	0.25(1)	0.50(2)	1.9(0.4)
$(1^+;0) \to (2^+;0)$	0.018(3)	0.021(3)		$18.15 \to 3.03$	0.06(1)	0.13(2)	4.3(1.2)
$[431] \to [44]$							
$(1^+;1) \to (2_2^+;0)$	2.287(10)	2.910(13)	21%	$17.64 \to 16.626$	1.92(2)[−2]	2.97(3)[−2]	3.2(3)[−2]
$(1^+;1) \to (2^+;1)$	0.139(2)	0.176(3)	21%	$17.64 \to 16.922$	1.22(3)[−3]	2.20(5)[−3]	1.3(3)[−3]
$(1^+;0) \to (2_2^+;0)$	0.167(3)	0.189(3)	12%	$18.15 \to 16.626$	2.52(3)[−2]	2.87(3)[−2]	7.7(1.9)[−2]
$(1^+;0) \to (2^+;1)$	2.596(11)	2.887(13)	10%	$18.15 \to 16.922$	3.26(3)[−2]	4.18(3)[−2]	6.2(7)[−2]
$[431] \to [431]$							
$(3^+;1) \to (2^+;0)$	0.386(13)	0.622(22)	38%	$19.070 \to 3.03$	0.87(6)	2.3(2)	10.5
$(3^+;0) \to (2^+;0)$	0.015(1)*	0.030(1)*		$19.235 \to 3.03$	0.15(2)	0.37(4)	–
$[431] \to [44]$							
$(0^+;2) \to (1^+;1)$	0.793(7)	1.095(8)	28%	$27.49 \to 17.64$	6.7(1)	12.7(2)	21.9(3.9)
$(0_3^+;0) \to (1^+;1)$	0.553(3)†	0.689(3)†	21%		8.3(3)†	15.5(5)†	
$(0_3^+;0) \to (1^+;0)$	0.073(1)†	0.082(1)†	11%	$27.49 \to 18.15$	0.28(1)†	0.54(1)†	–
$[422] \to [431]$							

isospin-mixed $M1$ transition matrix elements:

$$\begin{aligned}
\langle \Psi^a_{J_f} || M1 || \Psi^a_{J_i} \rangle &= \alpha_{J_f}\alpha_{J_i} M1_{00} + \alpha_{J_f}\beta_{J_i} M1_{01} \\
&\quad + \beta_{J_f}\alpha_{J_i} M1_{10} + \beta_{J_f}\beta_{J_i} M1_{11}, \\
\langle \Psi^b_{J_f} || M1 || \Psi^a_{J_i} \rangle &= \beta_{J_f}\alpha_{J_i} M1_{00} + \beta_{J_f}\beta_{J_i} M1_{01} \\
&\quad - \alpha_{J_f}\alpha_{J_i} M1_{10} - \alpha_{J_f}\beta_{J_i} M1_{11}, \\
\langle \Psi^a_{J_f} || M1 || \Psi^b_{J_i} \rangle &= \alpha_{J_f}\beta_{J_i} M1_{00} - \alpha_{J_f}\alpha_{J_i} M1_{01} \\
&\quad + \beta_{J_f}\beta_{J_i} M1_{10} - \beta_{J_f}\alpha_{J_i} M1_{11}, \\
\langle \Psi^b_{J_f} || M1 || \Psi^b_{J_i} \rangle &= \beta_{J_f}\beta_{J_i} M1_{00} - \beta_{J_f}\alpha_{J_i} M1_{01} \\
&\quad - \alpha_{J_f}\beta_{J_i} M1_{10} + \alpha_{J_f}\alpha_{J_i} M1_{11}. \qquad (24)
\end{aligned}$$

The isospin-mixed $M1$ matrix elements are used to evaluate the widths as given in Eq. (17) for comparison to experiment. The IA and total values are reported in the sixth and seventh columns in Table III, and the experimental widths (where available) are listed in the last column.

Three extra transitions that were calculated only in the VMC are followed by a superscript asterisk or dagger in Table III; they may affect the physical decay widths through isospin mixing. The $(3^+;0) \to (2^+;0)$ transition, followed by a superscript asterisk, is tiny and its isospin mixing has little effect on the transition from the physical 19.07-MeV state. The corresponding transition from the 19.235-MeV state is predicted to be much smaller and has not been reported experimentally. Perhaps more interesting and important, although speculative, is the isospin mixing of the proposed $(0_3^+;0)$ state, discussed at the end of Sec. III, into the physical 27.49-MeV state, as listed in the second- and next-to-last rows in Table III followed by a superscript dagger. The row above these lists the results assuming that the physical state is pure $T = 2$, and even with MEC contributions, the theoretical width is noticeably underpredicted. The first row with daggers shows that mixing in the $(0_3^+;0)$ state, using $\alpha_0 = 0.19(4)$, increases the decay width by 20%, bringing it closer to experiment. The final line shows the corresponding decay to the 18.15-MeV state as much smaller and thus unlikely to be observed. A fourth possible transition in this group, $(0^+;2) \to (1^+;0)$, has $\Delta T = 2$ and vanishes in IA and also for the MEC considered in this paper.

The $M1$ transitions listed in Table III can be sorted into four categories, characterized by having large, medium, small, and tiny matrix elements. The two largest matrix elements are between states of the same spatial symmetry that change isospin: $(1^+;1) \to (2_2^+;0)$ and $(1^+;0) \to (2^+;1)$. All four states involved have predominant [431] spatial symmetry, so there is maximum overlap between the w.f.'s. Further, because $\Delta T = 1$, the spin-magnetization terms of the protons and neutrons add constructively. This feature is illustrated in Figs. 5(a) and 5(b), where we plot the IA contributions

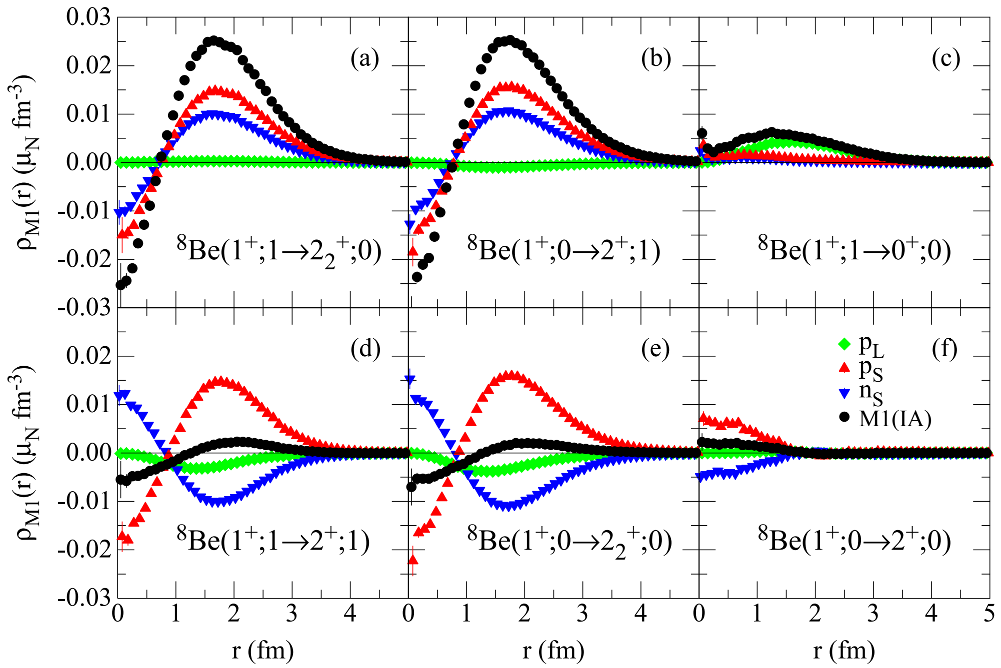

FIG. 5. (Color online) One-body (IA) $M1$ transition density (in μ_N per fm^3) for selected $M1$ transitions (see text for explanation).

to the magnetic transition density from Eq. (21), evaluated with the starting VMC w.f.'s. In the figure, upward-pointing (red) triangles show the proton spin contribution, downward-pointing (blue) triangles show the neutron spin contribution, (green) diamonds are the proton orbital term, and black circles represent the total transition density. In both these transitions, the spin contributions are large and the proton orbital piece is very small, resulting in a total matrix element of $\sim 3.0\ \mu_N$.

There are also two transitions between states of the same spatial symmetry where isospin is conserved, i.e., $\Delta T = 0$, which results in small matrix elements: $(1^+;1) \rightarrow (2^+;1)$ and $(1^+;0) \rightarrow (2_2^+;0)$. These are illustrated in Figs. 5(d) and 5(e). The magnitudes of the proton spin and neutron spin contributions are very similar to the $\Delta T = 1$ case, but they have opposite signs and cancel against each other, and there is a more substantial proton orbital term, which further reduces the total, leading to matrix elements of $\sim 0.2\ \mu_N$. The values of the VMC densities integrated over d^3r are listed in Table IV for the transitions shown in Figs. 5(a) and 5(d).

Next, there are five matrix elements which are between states of different spatial symmetry and are $\Delta T = 1$ transitions, such as the $(1^+;1) \rightarrow (0^+;0)$ transition illustrated in the Fig. 5(c). These transitions have proton and neutron spin contributions that add coherently but are small because of the small overlap of the initial and final w.f.'s. However, they have larger proton orbital pieces, which also add coherently and dominate the total, leading to medium-size matrix elements, in the range 0.5–1.0 μ_N.

Finally, there are three matrix elements between states of different spatial symmetries that have $\Delta T = 0$, and these are tiny. An example is the $(1^+;0) \rightarrow (2^+;0)$ transition in Fig. 5(f). In these cases the proton and neutron spin terms are small in magnitude and of opposite sign, and the proton orbital piece is also very small, resulting in matrix elements $<0.03\ \mu_N$.

The net contribution of MEC EM currents (where MEC = Total − IA) is best appreciated by looking at matrix elements between states with well-defined isospins, as listed in the second to fourth columns in Table III. The quantity z in the fourth column is the percentage contribution of the MEC to the total; it is not given if the MEC is less than the statistical error of the total. MEC contributions to $\Delta T = 0$ transitions are generally smaller than $\Delta T = 1$ transitions. This is due to the fact that the major MEC correction, given by the OPE seagull and pion-in-flight terms at NLO, is purely isovector and cannot contribute to $\Delta T = 0$ transitions. Therefore, only higher order terms, i.e., terms at N2LO and N3LO, contribute to these matrix elements, for which we find $z \sim 10\%$. Transitions induced by the isovector component of the M1 operator, that is, transitions in which $T_i \neq T_f$, are instead characterized by a z factor spanning the interval ~20%–40%. In general, the NLO currents of one-pion range provide ~60%–70% of the total MEC correction. In Table III, we see that the contribution given by the MEC currents (with only one exception) improves the IA values, bringing the theory into better agreement with the experimental data.

It is also interesting to examine the transition magnetic densities due to MEC. As examples, we discuss the same six transitions whose IA densities are given in Fig. 5. The associated two-body magnetic densities obtained from MEC terms are shown in Fig. 6, again as calculated with the starting VMC w.f.'s. For Figs. 6(a)–6(c), which are isovector transitions, the (red) circles labeled NLO-OPE show the density due to the long-ranged OPE currents, while corrections associated with TPE currents at N3LO are represented by the (cyan) squares

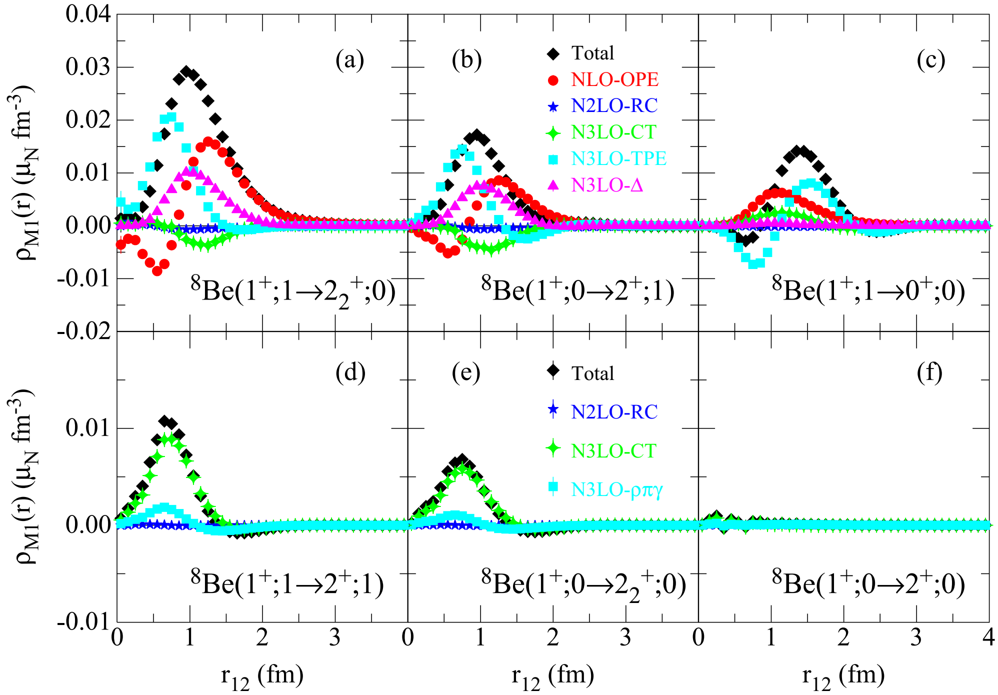

FIG. 6. (Color online) Two-body (IA) $M1$ transition density (in μ_N per fm^3) for selected $M1$ transitions (see text for explanation).

labeled N3LO-TPE. Contact current contributions, of both minimal and nonminimal nature, are represented by the (green) four-pointed stars labeled N3LO-CT, while the contribution due to the current in the one-pion range, which has been saturated by the Δ resonance, is represented by the (magenta) triangles labeled N3LO-Δ. In the figure, we also show, with (blue) five-pointed stars labeled N2LO-RC, the one-body relativistic correction given in Eq. (22). The black diamonds represent the sum of the various contributions. The tail of the magnetic distribution is dominated by the long-range OPE contribution, followed by the N3LO-Δ one; at intermediate to short range, TPE contributions become important. The integrated values of the individual MEC contributions to the $(1^+;1) \rightarrow (2_2^+;0)$ isovector transition [Fig. 6(a)] are listed in Table IV.

TABLE IV. Individual IA and MEC contributions to one isovector and one isoscalar $M1$ transition matrix elements (in μ_N) calculated in the VMC, corresponding to Figs. 5(a) and 5(d) and 6(a) and 6(d).

$(J_i,T_i) \rightarrow (J_f,T_f)$	$(1^+;1) \rightarrow (2_2^+;0)$	$(1^+;1) \rightarrow (2^+;1)$
IA		
p_L	0.031(1)	−0.224(1)
p_S	1.442(7)	1.267(7)
n_S	0.988(5)	−0.867(5)
IA total	2.461(13)	0.176(3)
NLO OPE	0.457(1)	
N2LO RC	−0.059(1)	−0.001
N3LO		
TPE	0.090(1)	
CT	−0.038(1)	0.040(1)
Δ	0.160(1)	
$\rho\pi\gamma$		−0.008
MEC total	0.610(2)	0.031(1)

Two-body magnetic densities for the isoscalar transitions are shown in Figs. 6(d)–6(f). The isoscalar component of the $M1$ operator has a rather different structure in comparison with that of its isovector component; it has no contributions at NLO, therefore isoscalar transitions are suppressed with respect to isovector ones. The first correction beyond the IA picture enters at N2LO and is given by the one-body relativistic correction of Eq. (22), shown by the (blue) five-pointed stars labeled N2LO-RC. There are two isoscalar contributions at N3LO. The first is associated with the tree-level current of one-pion range represented by the (cyan) squares labeled N3LO-$\rho\pi\gamma$. This isoscalar tree-level current can, in principle, be saturated by the $\rho\pi\gamma$ transition current [20], however, we fix its associated LEC so as to reproduce the magnetic moments of the deuteron and the isoscalar combination of the trinucleon magnetic moments, as explained in Sec. II. The second is the contact current at N3LO, shown by the (green) four-pointed stars labeled N3LO-CT, and these, in fact, dominate the total isoscalar two-body MEC contribution shown by the black diamonds. The integrated values for the $(1^+;1) \rightarrow (2^+;1)$ transition [Fig. 6(d)] are also listed in Table IV.

V. DISCUSSION

The spatial symmetry-conserving $M1$ transitions are between the isospin-mixed 2^+ and 1^+ doublets, so comparison with experimental widths requires both the matrix elements between isospin-pure states and the α_J and β_J parameters of

TABLE V. Effect of alternate isospin-mixing coefficient α_1 on Γ_{M1}; the notation $[-x] = 10^{-x}$.

	Γ_{M1} (eV)		
$E_i \rightarrow E_f$ (MeV)	$\alpha_1 = 0.21$	$\alpha_1 = 0.31$	Expt.
17.64 → 0.00	12.0(3)	11.4(3)	15.0(1.8)
17.64 → 3.03	3.8(2)	3.6(2)	6.7(1.3)
18.15 → 0.00	0.50(2)	1.16(4)	1.9(0.4)
18.15 → 3.03	0.13(2)	0.32(3)	4.3(1.2)
[431] → [44]			
17.64 → 16.626	2.97(3)[–2]	3.28(3)[–2]	3.2(3)[–2]
17.64 → 16.922	2.20(5)[–3]	1.39(4)[–2]	1.3(3)[–3]
18.15 → 16.626	2.87(3)[–2]	1.84(2)[–2]	7.7(1.9)[–2]
18.15 → 16.922	4.18(3)[–2]	4.59(3)[–2]	6.2(7)[–2]
[431] → [431]			

Eqs. (13) and (14) as input. We consider α_2 and β_2 to be well determined by the Γ_α measurements for the 2^+ doublet. However, α_1 and β_1 were first estimated by Barker [29] by looking at the ratio of the Γ_{M1}'s for the 1^+ doublet and comparing it to shell-model calculations. Instead, we could use our more sophisticated calculations to determine the best isospin-mixing parameters.

If we minimize χ^2 with respect to experiment for the four spatial symmetry-conserving transitions, i.e., those given in the third group in Table III, we find $\alpha_1 = 0.31(4)$, compared to the "experimental" value of 0.21(3) used previously in Table III and discussed in Ref. [11]. The predicted widths for these two isospin-mixing parameters are compared in Table V, along with the four other symmetry-changing transitions from the 1^+ doublet to the ground or first excited state; the χ^2 comparison with experiment for these cases is also improved. However, this alternate value for α_1 implies a significantly larger isospin-mixing matrix element, $H_{01} = -150(18)$ keV, compared to the theoretical value for this Hamiltonian of $-94(1)$ keV calculated in Ref. [11], which was in good agreement with the earlier empirical value of $-103(14)$ keV.

The results of our QMC calculations are in fair agreement with experiment when the transitions are between states of the same spatial symmetry. However, when the spatial symmetry of the initial and final states is different, we generally underpredict the reported experimental widths. The $E2$ calculations in Table II give large matrix elements for the [44] → [44] transitions and show reasonable agreement with the recently remeasured $(4^+;0) \rightarrow (2^+;0)$ width. The calculations underpredict the [44] → [431] transitions from the isospin-mixed 2^+ doublet to the ground state, although here both theory and experiment have large error bars. The predicted transitions to the first 2^+ are smaller and, perhaps not surprisingly, unobserved to date. For the $E2$ transition from the first 1^+ at 17.64 MeV, we significantly overpredict the width, due to the surprisingly large $\Delta T = 1$ matrix element between $^1D[44]$ and $^1P[431]$ symmetry components. The unobserved transition from the 1^+ state at 18.15 MeV is tiny, due to a vanishing $\Delta T = 0$ matrix element. The larger value of α_1 discussed above would reduce the discrepancy with experiment slightly.

The QMC results for $M1$ matrix elements are similar, in that the four symmetry-conserving [431] → [431] transitions are in fair agreement with experiment, once MEC contributions are included. The agreement can be improved further by searching for better isospin-mixing parameters, α_J and β_J, as discussed above. Seven of the eight symmetry-changing $M1$ transitions are underpredicted by amounts ranging from only 25% to factors of 2–5. The worst matrix element is the same $(1^+;0) \rightarrow (2^+;0)$ transition that also vanishes in $E2$, leading to a decay width for the 18.15-MeV state which is 15–30 times too small.

Even though many of the experimental widths considered in this work have large errors, the serious discrepancies between some of the experimental and the calculated values highlight the challenge for theory to accurately predict transition amplitudes between states with dominant admixtures of different spatial symmetry or between states consisting of linear combinations of components of different spatial symmetry and occurring with similar probabilities.

Another possible source of difficulty is that we treat all the states in ^{8}Be as particle stable, without a continuum component. We believe this is a good approximation for the physically narrow states, but it is more questionable for wide states like the first $(2^+;0)$ and $(4^+;0)$. As noted in Ref. [10], it would be better to treat the latter states as true α-α scattering states, analogous to the neutron-α scattering description of ^{5}He [33]. (This could also be important for the eventual evaluation of weak decays of ^{8}Li and ^{8}B, which both go to the ^{8}Be $(2^+;0)$ state.) This will have to be addressed in future work.

To our knowledge, Refs. [1] and [2] and the present work are the only *ab initio* calculations of EM transitions in $A > 4$ nuclei that include MEC contributions. We find that the calculated $M1$ matrix elements have significant contributions, typically at the 20%–30% level, from two-body EM current operators, especially from those of one-pion range. The sizable MEC corrections are found to almost always improve the IA results for $M1$ transitions. This corroborates the importance of many-body effects in nuclear systems and indicates that an understanding of low-energy EM transitions requires contributions from MECs in combination with a complete treatment of nuclear dynamics based on Hamiltonians that include two- and three-nucleon forces.

ACKNOWLEDGMENTS

The many-body calculations were performed on the parallel computers at the Laboratory Computing Resource Center, Argonne National Laboratory. This work was supported by the National Science Foundation, Grant No. PHY-1068305 (S.P.), and by the US Department of Energy, Office of Nuclear Physics, under Contracts No. DE-FG02-09ER41621 (S.P.), No. DE-AC02-06CH11357 (S.C.P. and R.B.W.) and No. DE-AC05-06OR23177 (R.S.) and under the NUCLEI SciDAC-3 grant.

[1] S. Pastore, S. C. Pieper, R. Schiavilla, and R. B. Wiringa, Phys. Rev. C **87**, 035503 (2013).

[2] L. E. Marcucci, M. Pervin, S. C. Pieper, R. Schiavilla, and R. B. Wiringa, Phys. Rev. C **78**, 065501 (2008).

[3] L. E. Marcucci, M. Viviani, R. Schiavilla, A. Kievsky, and S. Rosati, Phys. Rev. C **72**, 014001 (2005).

[4] S. Pastore, R. Schiavilla, and J. L. Goity, Phys. Rev. C **78**, 064002 (2008).

[5] S. Pastore, L. Girlanda, R. Schiavilla, M. Viviani, and R. B. Wiringa, Phys. Rev. C **80**, 034004 (2009).

[6] M. Piarulli, L. Girlanda, L. E. Marcucci, S. Pastore, R. Schiavilla, and M. Viviani, Phys. Rev. C **87**, 014006 (2013).

[7] R. B. Wiringa, V. G. J. Stoks, and R. Schiavilla, Phys. Rev. C **51**, 38 (1995).

[8] S. C. Pieper, AIP Conf. Proc. **1011**, 143 (2008).

[9] R. B. Wiringa, S. C. Pieper, J. Carlson, and V. R. Pandharipande, Phys. Rev. C **62**, 014001 (2000).

[10] V. M. Datar *et al.*, Phys. Rev. Lett. **111**, 062502 (2013).

[11] R. B. Wiringa, S. Pastore, S. C. Pieper, and Gerald A. Miller, Phys. Rev. C **88**, 044333 (2013).

[12] R. B. Wiringa, Phys. Rev. C **43**, 1585 (1991).

[13] B. S. Pudliner, V. R. Pandharipande, J. Carlson, S. C. Pieper, and R. B. Wiringa, Phys. Rev. C **56**, 1720 (1997).

[14] N. Metropolis, A. W. Rosenbluth, M. N. Rosenbluth, A. H. Teller, and E. Teller, J. Chem. Phys. **21**, 1087 (1953).

[15] J. Carlson, Phys. Rev. C **36**, 2026 (1987); **38**, 1879 (1988).

[16] G. P. Kamuntavičius, P. Navrátil, B. R. Barrett, G. Sapragonaite, and R. K. Kalinauskas, Phys. Rev. C **60**, 044304 (1999).

[17] M. Pervin, S. C. Pieper, and R. B. Wiringa, Phys. Rev. C **76**, 064319 (2007).

[18] T.-S. Park, D.-P. Min, and M. Rho, Nucl. Phys. A **596**, 515 (1996).

[19] S. Kölling, E. Epelbaum, H. Krebs, and U.-G. Meissner, Phys. Rev. C **80**, 045502 (2009); **84**, 054008 (2011).

[20] S. Pastore, L. Girlanda, R. Schiavilla, and M. Viviani, Phys. Rev. C **84**, 024001 (2011).

[21] D. R. Entem and R. Machleidt, Phys. Rev. C **68**, 041001 (2003).

[22] R. Machleidt and D. R. Entem, Phys. Rep. **503**, 1 (2011).

[23] Y.-H. Song, R. Lazauskas, T.-S. Park, and D.-P. Min, Phys. Lett. B **656**, 174 (2007).

[24] Y.-H. Song, R. Lazauskas, and T.-S. Park, Phys. Rev. C **79**, 064002 (2009).

[25] R. Lazauskas, Y.-H. Song, and T.-S. Park, Phys. Rev. C **83**, 034006 (2011).

[26] L. Girlanda, A. Kievsky, L. E. Marcucci, S. Pastore, R. Schiavilla, and M. Viviani, Phys. Rev. Lett. **105**, 232502 (2010).

[27] D. R. Tilley, J. H. Kelley, J. L. Godwin, D. J. Millener, J. E. Purcell, C. G. Sheu, and H. R. Weller, Nucl. Phys. A **745**, 155 (2004).

[28] V. M. Datar, S. Kumar, D. R. Chakrabarty, V. Nanal, E. T. Mirgule, A. Mitra, and H. H. Oza, Phys. Rev. Lett. **94**, 122502 (2005).

[29] F. C. Barker, Nucl. Phys. **83**, 418 (1966).

[30] E. A. McCutchan *et al.*, Phys. Rev. C **86**, 014312 (2012).

[31] S. C. Pieper, R. B. Wiringa, and J. Carlson, Phys. Rev. C **70**, 054325 (2004).

[32] R. B. Wiringa, Phys. Rev. C **73**, 034317 (2006).

[33] K. M. Nollett, S. C. Pieper, R. B. Wiringa, J. Carlson, and G. M. Hale, Phys. Rev. Lett. **99**, 022502 (2007).